J Adv Ceram

Research Article

Microstructure and thermal properties of hafnium-doped high-entropy oxide $(Y_{0.25}Ho_{0.25}Er_{0.25}Yb_{0.25})_2O_3$ coatings

Guangheng Zhang[1], Huiming Wang[1], Xin Li[1], Luchao Sun[2], Jie Zhang[2], Huiming Guo[3,✉], Jingyang Wang[1,2,✉]

Cite this article: Zhang G, Wang H, Li X, et al. *J Adv Ceram* 2026, **15**(3): 9221250. https://doi.org/10.26599/JAC.2026.9221250

ABSTRACT: The development of thermal/environmental barrier coatings (T/EBCs) is significantly constrained by the stringent material requirements for their topcoats. This study explores the implications of hafnium oxide (HfO_2) doping on the crystal structure and thermophysical properties of high-entropy $(Y_{0.25}Ho_{0.25}Er_{0.25}Yb_{0.25})_2O_3$ oxide, with the goal of designing and selecting novel topcoat materials. $(RE_{1-x}Hf_x)_2O_{3+x}X_{1-x}$ (RE = $Y_{0.25}Ho_{0.25}Er_{0.25}Yb_{0.25}$; X = oxygen vacancy) coatings with 5, 10, 20, and 50 mol% hafnium oxide were deposited by atmospheric plasma spraying (APS). Systematic investigations were conducted on their hardness, Young's modulus, phase composition, phase stability, thermal conductivity, and coefficient of thermal expansion. At lower HfO_2 doping contents (5–20 mol%), the $(RE_{1-x}Hf_x)_2O_{3+x}X_{1-x}$ coatings retained the bixbyite structure, whereas the higher HfO_2 doping level (50 mol%) induced a phase transition to the fluorite structure. The structural evolution is attributed to the ordered arrangement of oxygen anions and vacancies in the crystal structure, which enhances the phase stability and simultaneously reduces the thermal conductivity but increases the hardness, Young's modulus and thermal expansion coefficient. The thermophysical properties of the $(RE_{1-x}Hf_x)_2O_{3+x}X_{1-x}$ coatings were strongly dependent on the HfO_2 doping content. The establishment of composition–structure–property relationships in the $(Y_{0.25}Ho_{0.25}Er_{0.25}Yb_{0.25})_2O_3$–$HfO_2$ system provides critical insights for the optimization of T/EBC materials in extreme environments.

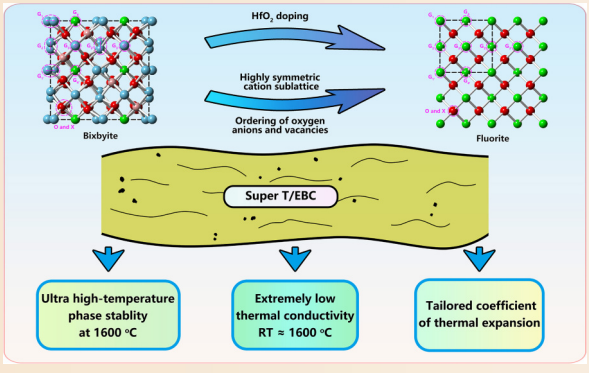

KEYWORDS: thermal/environmental barrier coatings (T/EBCs); $(RE_{1-x}Hf_x)_2O_{3+x}X_{1-x}$ coatings; bixbyite structure; fluorite structure; thermophysical properties

1 Introduction

Silicon carbide fiber-reinforced silicon carbide ceramic matrix composites (SiC_f/SiC CMCs) exhibit an exceptional combination of low density and superior high-temperature performance, establishing them as ideal material candidates for advanced aircraft engine hot-section components [1]. During aircraft engine service, the critical hot-section components face severe degradation from corrosive environments, including high-temperature steam and molten calcium–magnesium–aluminosilicate (CaO–MgO–Al_2O_3–SiO_2, CMAS) deposits. The deposition of an environmental barrier coating (EBC) serves as an effective solution [2,3]. As thrust-to-weight ratios rise in advanced aircraft engines, the wall temperature of high-pressure turbine components reaches up to 1500 °C, significantly surpassing the temperature resistance limit of SiC_f/SiC CMCs, 1350–1400 °C. Therefore, an additional deposition of a thermal barrier coating (TBC) over an existing EBC could simultaneously provide corrosion resistance and enhanced thermal protection, ensuring the high reliability of hot-section components throughout their service [4,5].

T/EBCs were conceptualized by Spitsberg *et al.* [6]. Through continuous research and development, the modern T/EBC system has evolved into a multilayer architecture comprising three primary functional layers: a bond coat, an intermediate coat, and a top coat, which is commonly prepared by atmospheric plasma spraying (APS) and/or electron beam physical vapor deposition (EB-PVD) [7,8]. The bond coat is mainly designed to enhance substrate adhesion and simultaneously serves as an oxygen barrier, primarily composed of Si or Si-hafnium oxide (Si-HfO_2). The intermediate coat, typically fabricated from rare earth silicates, functions as a diffusion barrier against gaseous or liquid corrosive media. The topcoat, as the primary interface with extreme service environments, imposes the most stringent requirements for

[1] Institute of Coating Technology for Hydrogen Gas Turbines, Liaoning Academy of Materials, Shenyang 110004, China. [2] Shenyang National Laboratory for Materials Science, Institute of Metal Research, Chinese Academy of Sciences, Shenyang 110016, China. [3] AECC Sichuan Gas Turbine Research Establishment, Chengdu 610500, China.

✉ Corresponding authors. E-mail: H. Guo, guohm633@aecc.com; J. Wang, jywang@imr.ac.cn

Received: September 18, 2025; Revised: December 9, 2025; Accepted: January 14, 2026

material selection. An ideal top coat material must exhibit not only exceptional high-temperature stability and thermal insulation properties but also excellent chemical and thermomechanical compatibility with the intermediate coat. Additionally, adequate corrosion resistance is another essential consideration. TBC materials have significantly evolved, progressing from traditional yttria-stabilized zirconia (YSZ) to advanced rare earth zirconates [9,10], aluminates [11,12], and tantalates [13]. However, owing to their physicochemical incompatibility with T/EBCs, these advanced materials have limited practical implementation.

Recently, high-entropy rare earth oxides have gained prominence as promising materials for TBCs owing to their superior high-temperature and corrosion resistance. Compared to single-component ceramics, high-entropy ceramics realize unique and unexpected properties arising from the synergistic effects of multiple components [14]. Rare earth oxides are particularly suited for high-entropy stabilization, as their inherent crystal structure demonstrates remarkable tolerance to variations in cation radius. Sun *et al.* [15] successfully synthesized cubic bixbyite-structure $(Eu_{0.2}Er_{0.2}Lu_{0.2}Y_{0.2}Yb_{0.2})_2O_3$ and $(Sm_{0.2}Er_{0.2}Lu_{0.2}Y_{0.2}Yb_{0.2})_2O_3$, with thermal conductivities ranging from 2.6 to 5.1 $W{\cdot}m^{-1}{\cdot}K^{-1}$ and thermal expansion coefficients of $(7.95–8.09)\times 10^{-6}$ K^{-1}. Their relatively low coefficients of thermal expansion imply good compatibility with the current T/EBC system. Ping *et al.* [16,17] synthesized a series of high-entropy rare earth oxide solid solutions, spanning from quaternary to decenary components. Their systematic investigations found that the quantity of rare earth constituents surpasses a critical threshold, and their effect on thermal conductivity reduction diminishes significantly. This phenomenon arises primarily from the limited lattice distortion caused by rare earth ions with similar sizes (0.868–1.032 Å) [18]. To achieve further thermal conductivity reduction, the introduction of dopant ions with substantially different sizes from the host rare earth ions appears necessary.

HfO_2 presents a very high melting point (2800 °C) [19], a low thermal conductivity, and a relatively low thermal expansion [20], which presents ideal characteristics for high-temperature coatings. The ionic radius of hafnium is considerably smaller than that of rare earth ions [18], leading to pronounced lattice distortion upon incorporation into host materials. Moreover, the substitution of tetravalent hafnium ions for trivalent rare earth ions generates extra point defects, which are expected to enhance phonon scattering and improve thermal insulation properties [21]. The RE_2O_3–HfO_2 system, including rare earth-doped hafnium oxides and stoichiometric rare earth hafnates, has been extensively investigated for TBC applications [5,8,22,23]. However, current investigations have disproportionately concentrated on high-HfO_2-content compositions, leaving a significant research gap in understanding the properties and potential applications of low-HfO_2 systems.

In this study, hafnium oxide was incorporated into a quaternary rare earth oxide solid solution $(Y_{0.25}Ho_{0.25}Er_{0.25}Yb_{0.25})_2O_3$, and the corresponding coatings were fabricated by APS. The effects of HfO_2 doping content on thermophysical properties were systematically investigated, which provided critical insights for optimizing the material selection of the top coat in T/EBCs.

2 Experimental

2.1 Feedstock preparation and coating deposition

The $(Y_{0.25}Ho_{0.25}Er_{0.25}Yb_{0.25})_2O_3$ powders were synthesized by the solid-state reaction method. High-purity commercial yttrium, holmium, erbium, and ytterbium oxides (> 99.9% purity, Dahua New Material Resources Co., Ltd., China) were precisely weighed according to the target stoichiometries, placed into Si_3N_4 containers, and ball-milled with ethanol medium for 24 h. After removing the ethanol, the mixtures were calcined in chamber furnaces at 1500 °C for 10 h. The $(Y_{0.25}Ho_{0.25}Er_{0.25}Yb_{0.25})_2O_3$ powders were combined with various contents of commercial HfO_2 powder (99.9% purity, Yaosheng Material Technology Co., Ltd., China), with subsequent ball milling performed to achieve homogeneous particle dispersion. The specific composition of mixed powders is shown in Table 1. For simplicity, the nomenclature 5Hf, 10Hf, 20Hf, and 50Hf was employed to distinguish these compositions. The spherical feedstocks were prepared by the spray drying method, utilizing water as the liquid phase medium and polyvinyl alcohol as the binder. The granulation process was conducted with the following optimized parameters: an air inlet temperature of 250 °C, an air outlet temperature of 120 °C, an atomizer rotational speed of 9000 $r{\cdot}min^{-1}$, and a spray dryer chamber internal pressure of −0.5 kPa.

5Hf, 10Hf, 20Hf, and 50Hf coatings were deposited on graphite substrates by an APS system equipped with an Axial III M600 Torch (Northwest Mettech, Surrey, Canada). Prior to coating, the graphite substrate underwent sandblasting pretreatment to achieve a surface roughness exceeding 5 μm, which was critical for ensuring optimal coating-substrate adhesion. To guarantee reliable estimation of subsequent thermodynamic properties, all coatings were prepared with a minimum thickness of 2 mm. Given the substantial thickness, coating deposition was conducted over a larger area (300 mm × 50 mm) to mitigate thermal stress accumulation. Representative optical images of the as-deposited coatings are provided in Fig S1 in the Electronic Supplementary Material (ESM). To isolate freestanding coatings, the graphite substrate was removed through its conversion to gaseous products by oxidation in air at 700 °C for 10 h. Subsequently, these coatings were annealed at 1200 °C for 20 h in an argon atmosphere to promote complete crystallization and enhance stability.

2.2 Thermodynamic property testing and sample characterization

The hardness and Young's modulus of the coatings were determined via a nanoindenter (G200X, KLA, USA) with continuous stiffness measurements. The quasistatic tests were conducted under an applied load of 50 mN, with a loading rate of

Table 1 Specific composition of $(Y_{0.25}Ho_{0.25}Er_{0.25}Yb_{0.25})_2O_3$ and HfO_2 mixed powders

Chemical composition (mol%)					Chemical formula	Abbreviation
$YO_{1.5}$	$HoO_{1.5}$	$ErO_{1.5}$	$YbO_{1.5}$	HfO_2		
23.75	23.75	23.75	23.75	5.00	$(Y_{0.2375}Ho_{0.2375}Er_{0.2375}Yb_{0.2375}Hf_{0.05})_2O_{3.05}$	5Hf
22.50	22.50	22.50	22.50	10.00	$(Y_{0.225}Ho_{0.225}Er_{0.225}Yb_{0.225}Hf_{0.1})_2O_{3.1}$	10Hf
20.00	20.00	20.00	20.00	20.00	$(Y_{0.2}Ho_{0.2}Er_{0.2}Yb_{0.2}Hf_{0.2})_2O_{3.2}$	20Hf
12.50	12.50	12.50	12.50	50.00	$(Y_{0.125}Ho_{0.125}Er_{0.125}Yb_{0.125}Hf_{0.5})_2O_{3.5}$	50Hf

100 mN·min^{-1} and a hold time of 1 s at peak load. To ensure statistical reliability, multiple indentations were performed at random locations on the polished cross-section of the coatings.

The 5Hf, 10Hf, 20Hf, and 50Hf coatings were isothermally annealed in chamber furnaces at 1600 °C for 20, 40, 60, 80, and 100 h to investigate the phase stability. The heating and cooling rates were 5 °C·min^{-1}. The strategic design of varied annealing durations allows for temporal tracking of potential phase transformation.

The thermal diffusivity (α) was measured by a laser flash analyzer (LFA 427, Netzsch, Germany) from room temperature to 1600 °C. Since the ceramic specimen is potentially semitransparent to the laser beam, its surface was coated with a thin layer of colloidal graphite to ensure opacity. However, at elevated temperatures, the graphite layer degrades upon direct contact with coatings, which leads to a sharp rise in thermal diffusivity measurements. To solve this issue, a thin platinum interlayer (2–3 μm) was deposited underneath the sprayed graphite. The thermal conductivity (κ) was obtained by the relation (Eq. (1)):

$$\kappa = \alpha c_p \rho \tag{1}$$

where the specific heat capacity (c_P) was calculated through Neumann–Kopp rules according to Ref. [24], and the density (ρ) was determined through Rietveld refinement of X-ray diffraction (XRD) patterns.

Thermal expansion measurements were conducted on a bar-shaped sample (2 mm × 2 mm × 20 mm) by a horizontal dilatometer (DIL832, TA, USA) in an argon atmosphere. The temperature was elevated from room temperature to 1500 °C at a heating rate of 5 °C/min, followed by furnace cooling. The linear coefficient of thermal expansion (α_L) was determined from the temperature-dependent linear expansion rate ($\Delta L/L$).

Phase composition was identified by an X-ray diffractometer (XRD; D8 Advance, Bruker, Germany) with Cu Kα radiation. Microstructure morphology was observed by a scanning electron microscope (SEM; Clara, Tescan, Czech Republic), while the chemical composition was determined by an energy-dispersive X-ray spectroscope (EDS; Ultim Max 100, Oxford, UK).

3 Results and discussion

3.1 Feedstocks

Figure 1 presents the phase structure analysis of $(Y_{0.25}Ho_{0.25}Er_{0.25}Yb_{0.25})_2O_3$ and HfO_2 powders, which are used as raw materials for the spray drying process. XRD analysis confirms that $(Y_{0.25}Ho_{0.25}Er_{0.25}Yb_{0.25})_2O_3$ adopts the cubic bixbyite structure (space group $Ia\bar{3}$, PDF#97-002-7775) following heat treatment at 1500 °C for 10 h, with complete solid solution formation evidenced by the absence of secondary phases and uniform peak shifts. The commercial HfO_2 powder predominantly consists of the monoclinic phase (space group $P2_1/c$, PDF#00-034-0104), with a minor fraction of the tetragonal phase (space group $P4_2/nmc$, PDF#97-017-3966). Their detailed crystallographic parameters are summarized in Table S1 in the ESM.

Figure 2 summarizes the surface and cross-section SEM micrographs of the 5Hf, 10Hf, 20Hf, and 50Hf feedstocks, along with their corresponding particle size distribution profiles. The surface morphology of feedstocks in Figs. 2(a)–2(d) reveals the following shape characteristics: The 10Hf and 20Hf feedstocks exhibit high sphericity, whereas the 5Hf and 50Hf feedstocks display reduced sphericity, with partial particles adopting a doughnut-like shape. From the cross-sectional perspective (Figs. 2(e)–2(h)), these four powders share remarkably similar microstructure features, including solid spheres, hollow spherical shells, doublets, and satellites, which are characteristic of particles generated by spray drying processes [25,26]. Laser particle size analysis confirms that all four feedstock powders follow log-normal distributions (Figs. 2(i)–2(l)), a characteristic attributed to stochastic droplet evaporation and aggregation processes during spray drying [27]. Furthermore, the particle size distribution range progressively narrows with increasing HfO_2 content. Compared with $(Y_{0.25}Ho_{0.25}Er_{0.25}Yb_{0.25})_2O_3$ powder, the high-density HfO_2 powder reduces the solid–liquid volume ratio within atomized droplets. This effect promotes liquid evaporation, resulting in greater volumetric shrinkage and ultimately yielding finer agglomerated particles. Moreover, the high-density powders possess a reduced specific surface area, low surface energy, and weak interparticle forces. These characteristics enhance slurry dispersion, leading to a more homogeneous powder distribution within the pulp suspension. As a result, particle agglomeration is significantly suppressed, and the formation of oversized particles is effectively prevented.

3.2 Freestanding coatings

Figures 3(a)–3(h) depict the microstructure of the as-prepared and annealed freestanding coatings with varying HfO_2 contents. Consistent with conventional APS coatings, all as-prepared freestanding coatings display the characteristic lamellar microstructure, containing limited porosity and microcracks, as shown in Figs. 3(a)–3(d). The microcrack density and dimensions

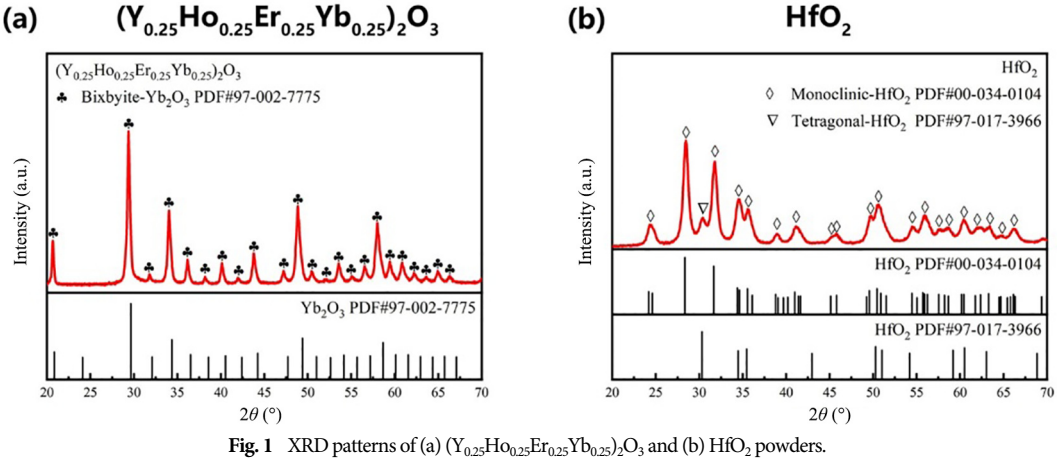

Fig. 1 XRD patterns of (a) $(Y_{0.25}Ho_{0.25}Er_{0.25}Yb_{0.25})_2O_3$ and (b) HfO_2 powders.

gradually increase with HfO_2 content, becoming particularly pronounced in the 50Hf coating. The phase diagram reveals that HfO_2 has a melting point approximately 300–400 °C higher than that of any individual component in $(Y_{0.25}Ho_{0.25}Er_{0.25}Yb_{0.25})_2O_3$ solid solution [19,28,29]. As the HfO_2 content increases, the elevated melting point of the feedstock powder leads to insufficient melting during spraying. The incomplete melting state promotes the formation of observable cracks within the coating.

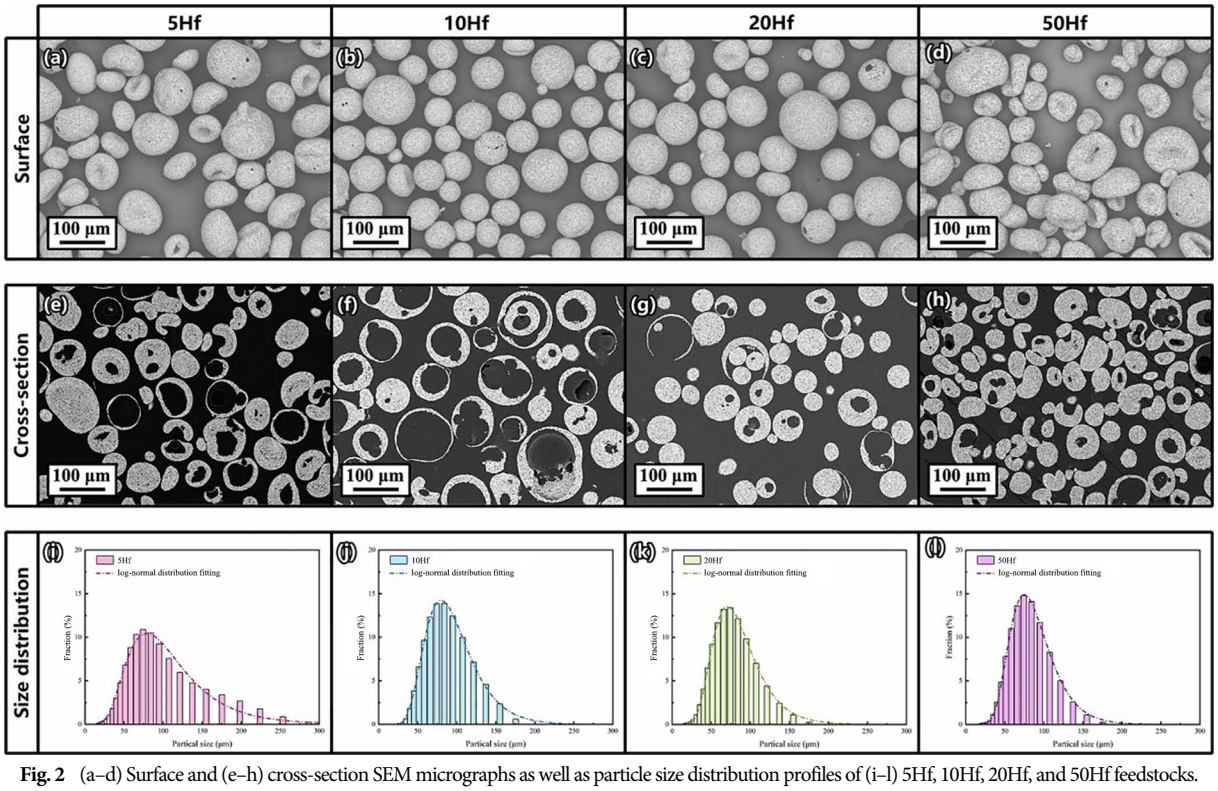

Fig. 2 (a–d) Surface and (e–h) cross-section SEM micrographs as well as particle size distribution profiles of (i–l) 5Hf, 10Hf, 20Hf, and 50Hf feedstocks.

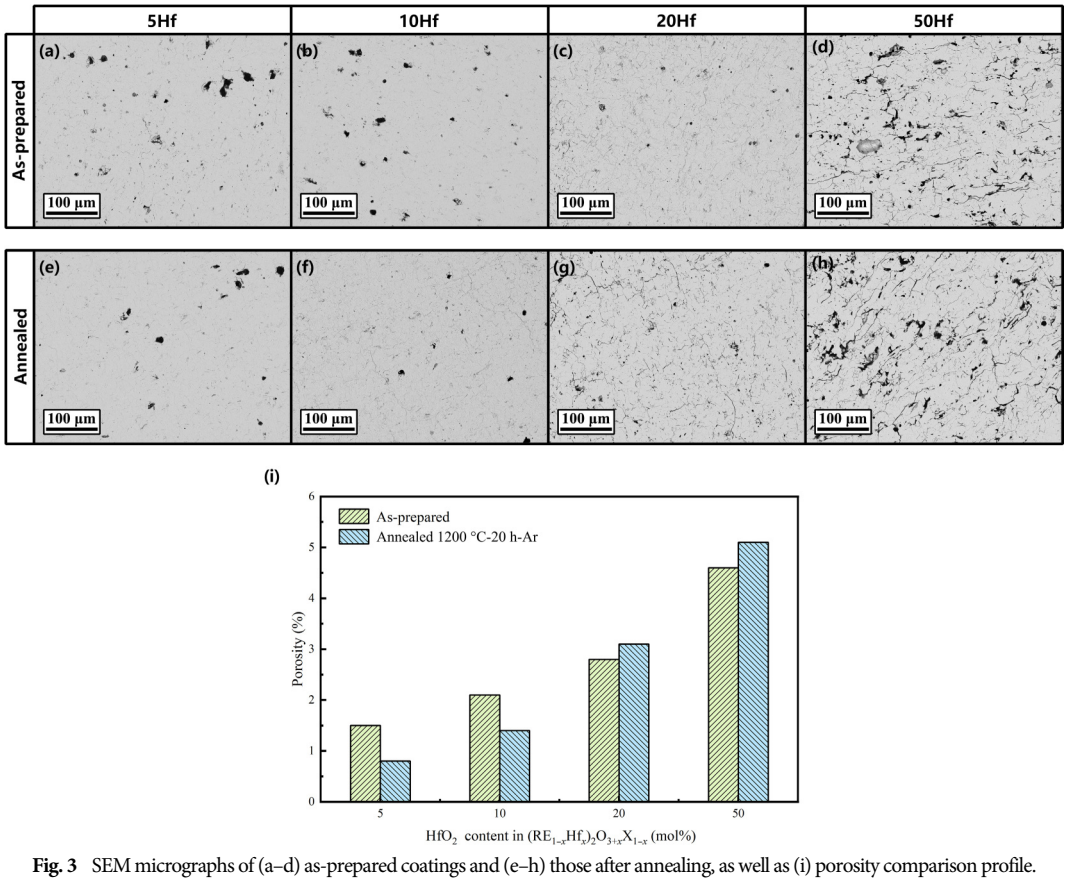

Fig. 3 SEM micrographs of (a–d) as-prepared coatings and (e–h) those after annealing, as well as (i) porosity comparison profile.

After heat treatment in an argon atmosphere at 1200 °C for 20 h, sintering effects led to a slight reduction in pore size in the freestanding coatings, as clearly observed in the 5Hf and 10Hf samples (Figs. 3(e) and 3(f)). However, an increased crack density is significantly observed in the 20Hf and 50Hf coatings (Figs. 3(g) and 3(h)). The thickness of these four freestanding coatings exceeds 2 mm; thus, considerable residual stresses accumulate during spraying. Subsequent stress relaxation during annealing promotes microcrack propagation. Figure 3(i) summarizes the porosity statistics (including cracks) for these four freestanding coatings in the as-prepared and annealed states. After annealing, the 5Hf and 10Hf coatings demonstrate a measurable reduction in porosity due to thermally induced pore shrinkage. In contrast, the 20Hf and 50Hf coatings demonstrate a modest porosity increase attributable to stress-induced crack propagation. The consistently low porosity (below 5.5%) across all freestanding coatings ensures the reliability of the subsequent thermophysical property evaluation. As shown in Table 2, the EDS analysis reveals excellent agreement between the measured coating compositions and their designed values. These findings indicate stable deposition without extra evaporation of any constituent during spraying.

Table 2 Measured compositions of 5Hf, 10Hf, 20Hf, and 50Hf annealed coatings

Smaple	Chemical composition (mol%, EDS)				
	$YO_{1.5}$	$HoO_{1.5}$	$ErO_{1.5}$	$YbO_{1.5}$	HfO_2
5Hf	23.1	23.3	24.1	24.1	5.3
10Hf	22.0	22.2	22.8	23.0	10.0
20Hf	19.4	20.0	20.6	20.0	19.9
50Hf	13.6	12.9	13.0	13.1	47.3

XRD patterns (Fig. 4) of the as-prepared freestanding coatings reveal that the $(Y_{0.25}Ho_{0.25}Er_{0.25}Yb_{0.25})_2O_3$ and HfO_2 feedstocks react completely across various ratios, forming single-phase solid solutions during plasma spraying. The coatings with low HfO_2 content (5Hf, 10Hf, and 20Hf) retain a cubic bixbyite structure, whereas diffraction peaks belonging to the fluorite phase with a space group of $Fm\bar{3}m$ are detected in the high-HfO_2 content coating (50Hf). The bixbyite-to-fluorite transition with HfO_2 content was also observed in the Gd_2O_3–HfO_2, Y_2O_3–HfO_2, and Lu_2O_3–HfO_2 systems reported by Sévin *et al.* [30]. The XRD patterns after annealing show that all coatings maintain their original phase structures without any observable transformation.

3.3 Structural comparison between bixbyite and fluorite

Bixbyite and fluorite both crystallize in the cubic system, sharing notable structural similarities [31]. The bixbyite structure is characterized by a relatively intricate cation distribution, with cations distributed between the high-symmetry 8b site and the low-symmetry 24d site, while anions exclusively populate the 48e position (Fig. 5(a)). Notably, the vacant 16c site in bixbyite can be viewed as an ordered arrangement of oxygen vacancies. In contrast, the fluorite structure demonstrates a face-centered cubic lattice with high symmetry, where cations occupy the 4a Wyckoff position and anions reside at the 8c site (Fig. 5(b)). The anionic sublattice in fluorite can accommodate oxygen vacancies to compensate for nonequivalent cation substitutions. In the two crystal structures, each cation is initially surrounded by eight anions, but the presence of anion vacancies leads to a variable coordination environment, with the effective number ranging from 6 to 8. The solid solution in the RE_2O_3–HfO_2 (RE = $Y_{0.25}Ho_{0.25}Er_{0.25}Yb_{0.25}$) system can be uniformly expressed as $(RE_{1-x}Hf_x)_2O_{3+x}X_{1-x}$, in which "X" represents oxygen vacancies.

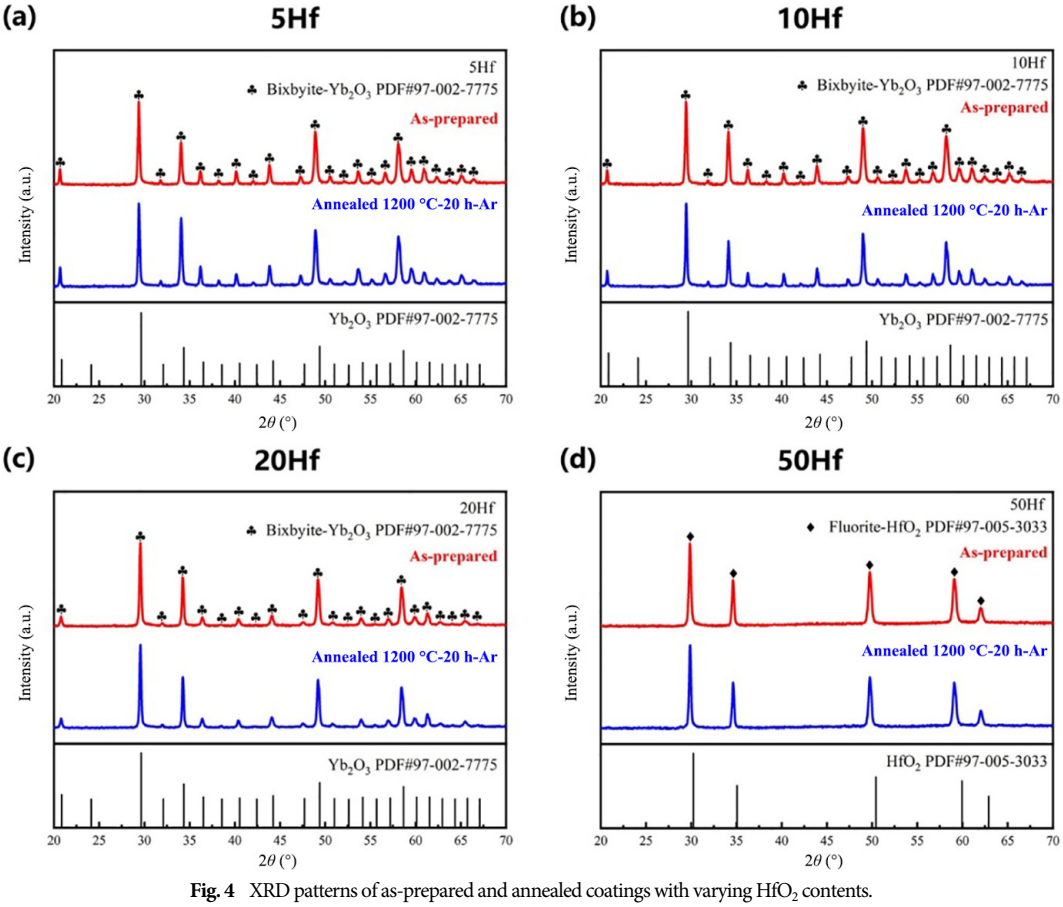

Fig. 4 XRD patterns of as-prepared and annealed coatings with varying HfO_2 contents.

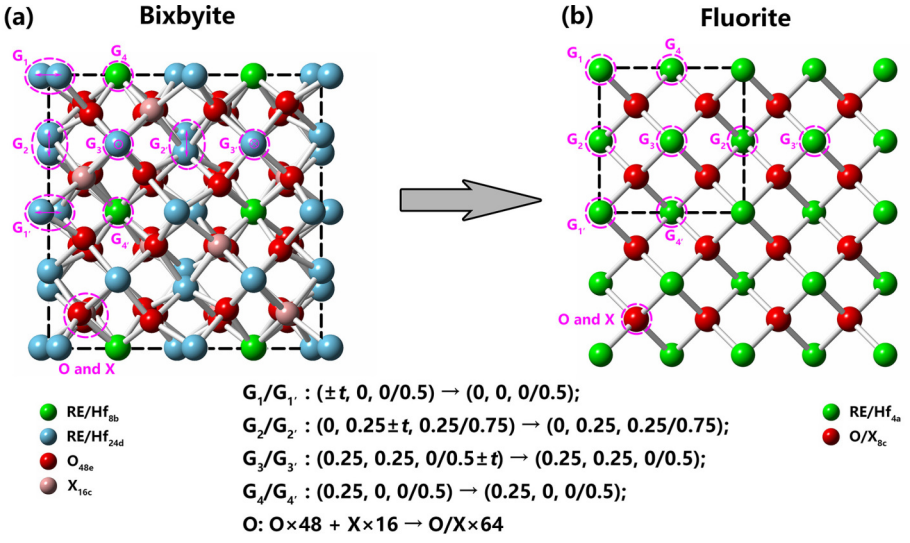

Fig. 5 Schematic representation of cation and anion sites in (a) bixbyite and (b) fluorite structures.

In the RE_2O_3–HfO_2 system, $(Y_{0.25}Ho_{0.25}Er_{0.25}Yb_{0.25})_2O_3$ exhibits a perfect bixbyite structure in the absence of HfO_2. When quadrivalent hafnium ions substitute for trivalent rare earth ions in the cation lattice, charge compensation requires the incorporation of additional oxygen ions into the anion lattice (occupying the 16c positions). The increased occupancy of oxygen ions at these 16c sites progressively destabilizes the bixbyite structure, eventually driving a phase transition to the more stable fluorite structure. The bixbyite-to-fluorite phase transformation involves systematic displacements of cations and anions. The cation sublattice in bixbyite can be partitioned into four distinct sites: $G_1/G_{1'}$, $G_2/G_{2'}$, $G_3/G_{3'}$, and $G_4/G_{4'}$ (Fig. 5(a)). During the transformation, the $G_1/G_{1'}$, $G_2/G_{2'}$, and $G_3/G_{3'}$ cations shift by a displacement distance "t" along the [100], [010], and [001] directions, respectively, whereas the $G_4/G_{4'}$ cations remain in their original positions (Fig. 5(b)). This displacement renders the $G_1/G_{1'}$, $G_2/G_{2'}$, and $G_3/G_{3'}$ sites structurally equivalent to the high-symmetry $G_4/G_{4'}$ site. The anionic sublattice undergoes a coordinated displacement toward higher-symmetry positions while simultaneously experiencing an order-disorder transition. The initially ordered arrangement of oxygen anions and vacancies in the bixbyite structure gives way to the characteristic disordered configuration of fluorite, with complete positional randomization. This disordering of oxygen anions and vacancies, which maximizes configurational entropy to overcome electrostatic interactions between cations and anions, emerges as the dominant thermodynamic driver for the phase transition. The resulting crystal structure displays a reduced repetition period, higher symmetry, and a lattice constant that is halved relative to the parent phase. The competitive relationship between ionic electrostatic interactions and configurational entropy governs the crystal structure of $(RE_{1-x}Hf_x)_2O_{3+x}X_{1-x}$.

To elucidate the detailed crystal structure of the RE_2O_3–HfO_2 sample, Rietveld refinement was performed on the XRD diffraction pattern. Figures 6(a)–6(d) present the refined diffraction patterns, demonstrating excellent agreement with the experimental data, as evidenced by reliability factors (R_{wp} < 16%, R_p < 11%) and a goodness-of-fit (χ^2 < 2). The refinement yielded comprehensive structural parameters, including lattice constants, RE/Hf atomic coordinates, oxygen positions, and theoretical density, all of which are systematically summarized in Table S2 in the ESM. The lattice constants of bixbyite-structured 5Hf, 10Hf, and 20Hf samples were determined to be 10.528, 10.513, and 10.474 Å, respectively, showing a progressive decrease with increasing HfO_2 content. In contrast, the fluorite-structured 50Hf sample exhibits a significantly reduced lattice constant of 5.183 Å, which is mainly attributed to the characteristic halving of lattice periodicity in the fluorite structure. For meaningful comparison between the two phases, the fluorite-phase lattice constant was normalized by doubling its value (Fig. 2(e)), enabling direct correlation analysis. A clear negative linear dependence of the lattice constant reduction on the HfO_2 doping content was observed across both structural phases, which is consistent with Vegard's law [32]. This systematic variation not only demonstrates the structural response to cation substitution but also highlights the close crystallographic relationship between bixbyite and fluorite phases. The observed lattice contraction can be primarily attributed to the substantial difference in ionic radii between the substituting cations: the tetravalent Hf ion (0.71 Å) is significantly smaller than the host trivalent rare earth ions (Y: 0.901 Å, Ho^{3+}: 0.901 Å, Er^{3+}: 0.89 Å, Yb^{3+}: 0.868 Å) [18]. While charge compensation through interstitial oxygen might be expected to partially offset the lattice contraction, the previous discussion indicates that these additional anions are effectively incorporated into the intrinsic vacancy sites of the bixbyite anion sublattice, consequently exerting only a minimal influence on the overall lattice parameters.

3.4 Mechanical performance

Hardness and Young's modulus are critical parameters that characterize a material's resistance to elastic and plastic deformation and serve as important indicators of coating performance. The nanoindentation technique derives these properties by analyzing the continuous load–displacement response during instrumented loading and unloading cycles (Fig. S2 in the ESM). Figure 7 compares the hardness and Young's modulus of the 5Hf, 10Hf, 20Hf, and 50Hf annealed coatings. As the HfO_2 doping content increases, the hardness exhibits a progressive rise from approximately 6.7±0.2 to 18.0±1.6 GPa, while the Young's modulus is promoted from approximately 118.4±7.6 to 229±10.0 GPa. The principal advantage of the nanoindentation method lies in the fact that the measured hardness and Young's modulus are extracted from a highly localized volume, effectively mitigating the influence of microstructural defects such as cracks, pores, and grain boundaries. As a result, the obtained data provide a more accurate

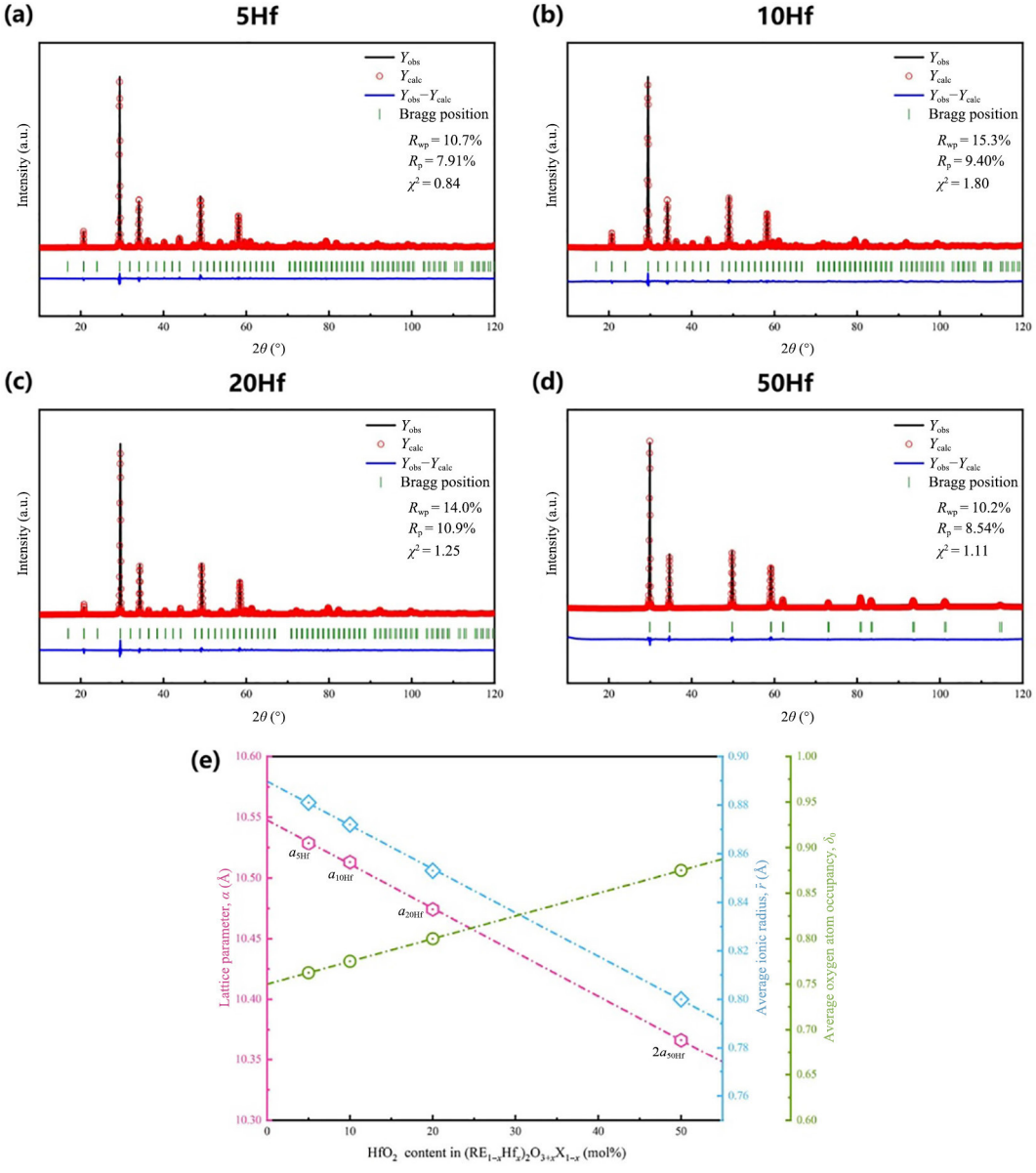

Fig. 6 (a–d) Rietveld refined XRD patterns of 5Hf, 10Hf, 20Hf, and 50Hf annealed coatings. (e) Variations in lattice parameter, average cation radius, and average oxygen anion occupancy with HfO_2 doping content.

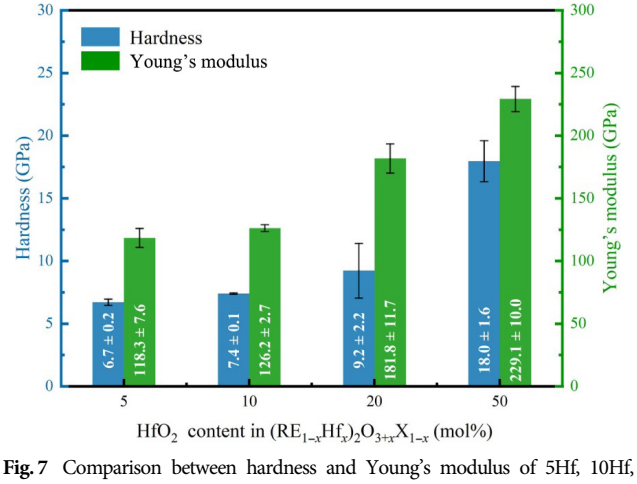

Fig. 7 Comparison between hardness and Young's modulus of 5Hf, 10Hf, 20Hf, and 50Hf annealed coatings.

intrinsic mechanical response of materials, which is governed by atomic bonding and crystal structure. As previously indicated, the structural similarity between bixbyite and fluorite phases renders the influence of crystal structure almost negligible. Hf ions exhibit a smaller ionic radius and a higher valence state than these rare earth ions. These characteristics collectively contribute to a substantially stronger Hf–O bond relative to RE–O bonds, which improves the deformation resistance of materials. Consequently, at a doping level of 50 mol% HfO_2, both the hardness and Young's modulus nearly double. The enhanced hardness and Young's modulus imply that the material, when employed as a topcoat, can more effectively resist severe mechanical damage.

3.5 High-temperature phase stability

Phase transformation and/or thermal decomposition within the coating could induce significant volumetric variation, which promotes microcrack initiation and interfacial delamination and ultimately accelerates coating failure. Exceptional high-temperature phase stability is critical for maintaining coating

structural integrity and ensuring reliable long-term performance in extreme environments. Figures 8(a)–8(d) display the XRD patterns of the 5Hf, 10Hf, 20Hf, and 50Hf coatings after heat treatment at 1600 °C in air for various durations. The 5Hf, 10Hf, and 20Hf coatings, which initially possessed a bixbyite structure, exhibited new diffraction peaks following heat treatment, indicating partial phase transformation. These additional peaks correspond to a novel hexagonal phase with the formula RE_6HfO_{11} (PDF#00-023-0974). Currently, investigations on this novel hexagonal structure remain limited, and its detailed structural characterization has yet to be explored. Nevertheless, it has been unequivocally established as an ordered phase in RE_2O_3–Zr/HfO_2 systems [19,33]. In contrast, the 50Hf coating retained its initial fluorite structure without detectable secondary phases even after prolonged high-temperature exposure. Interestingly, after removing the surface coating by grinding away several tens to hundreds of micrometers, XRD analysis of the underlying material revealed distinct phase compositions, as shown in Figs. 9(a)–9(d). The 5Hf, 10Hf, and 20Hf samples exclusively displayed diffraction peaks corresponding to the bixbyite phase, without phase transitions, whereas only the fluorite phase was observed in the 50Hf sample. This suggests that the bixbyite-to-RE_6HfO_{11} phase transformation is oxygen diffusion dependent. Environmental oxygen incorporation into the lattice modifies the local coordination environment, triggering cation ordering. This mechanism is very common in perovskite-structure and spinel-structure materials [34,35].

The fluorite phase demonstrates significantly superior high-temperature phase stability compared to the bixbyite phase. However, subtle differences in phase stability are also observed among the bixbyite phases with varying HfO_2 doping contents. XRD patterns under various heat treatment durations reveal distinct phase evolution trends among these samples. The 5Hf and 10Hf samples show clear diffraction peaks attributable to RE_6HfO_{11} after 20 h (Figs. 8(a) and 8(b)). In contrast, the 20Hf sample maintains its single-phase bixbyite structure over the same period, with RE_6HfO_{11} formation becoming evident after prolonging the heat treatment period to 40 h (Fig. 8(c)). This delayed phase transition suggests that increased HfO_2 doping content hinders atomic diffusion kinetics, thus retarding the bixbyite-to-RE_6HfO_{11} transformation. The bixbyite phase demonstrates progressively improved phase stability with higher HfO_2 incorporation.

The Gibbs free energy (G), a fundamental thermodynamic potential governing the phase stability of materials, is defined as Eq. (2):

$$G = H - TS \tag{2}$$

where H, T, and S denote enthalpy, absolute temperature and entropy, respectively. At low temperatures, the Gibbs free energy is predominantly enthalpy-driven, while entropy becomes the dominant factor at elevated temperatures. Entropy is a thermodynamic quantity that quantifies the degree of disorder or randomness in a system. The total entropy can be described as Eq. (3):

$$S = S_{\text{config}} + S_{\text{vib}} + S_{\text{elec}} \tag{3}$$

where S_{config} is the configurational entropy associated with atomic arrangements, S_{vib} is the vibrational entropy stemming from lattice vibrations, and S_{elec} is the electronic entropy derived from electron spin distributions and energy level occupations. Since $(RE_{1-x}Hf_x)_2O_{3+x}X_{1-x}$ solid solutions with different compositions share similar crystal structures and exhibit electronic insulating properties, the effects of electronic and vibrational entropy effects are negligible. Extensive research has explored the role of

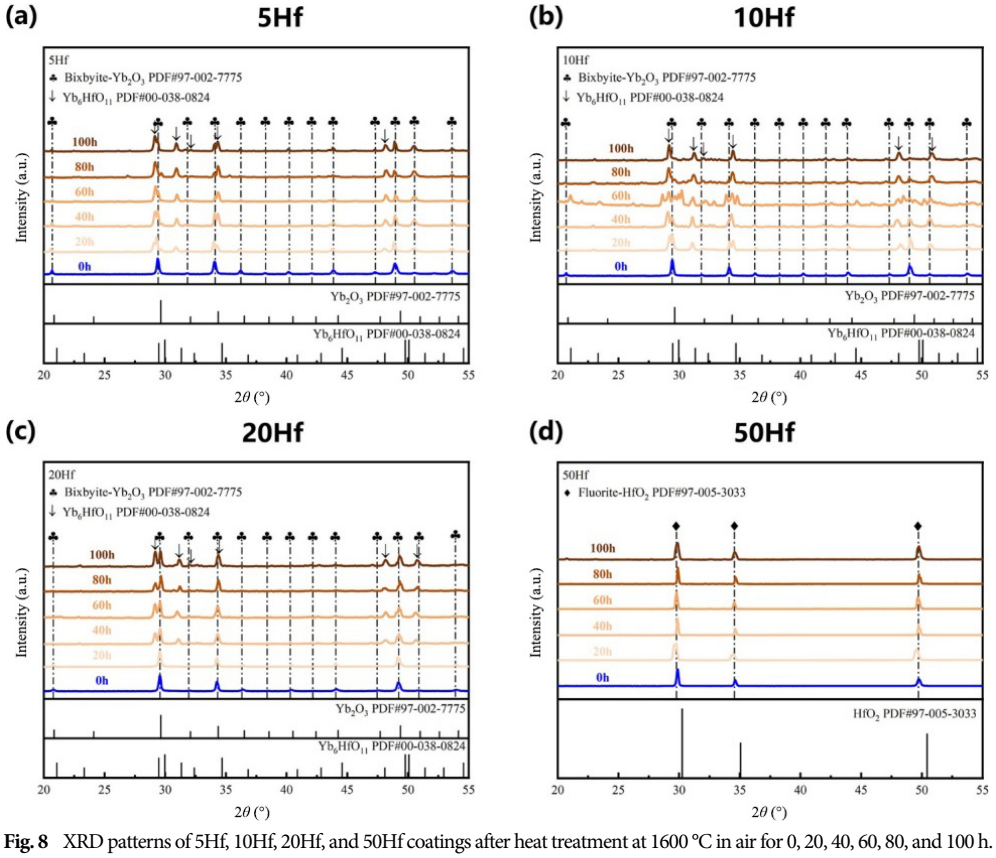

Fig. 8 XRD patterns of 5Hf, 10Hf, 20Hf, and 50Hf coatings after heat treatment at 1600 °C in air for 0, 20, 40, 60, 80, and 100 h.

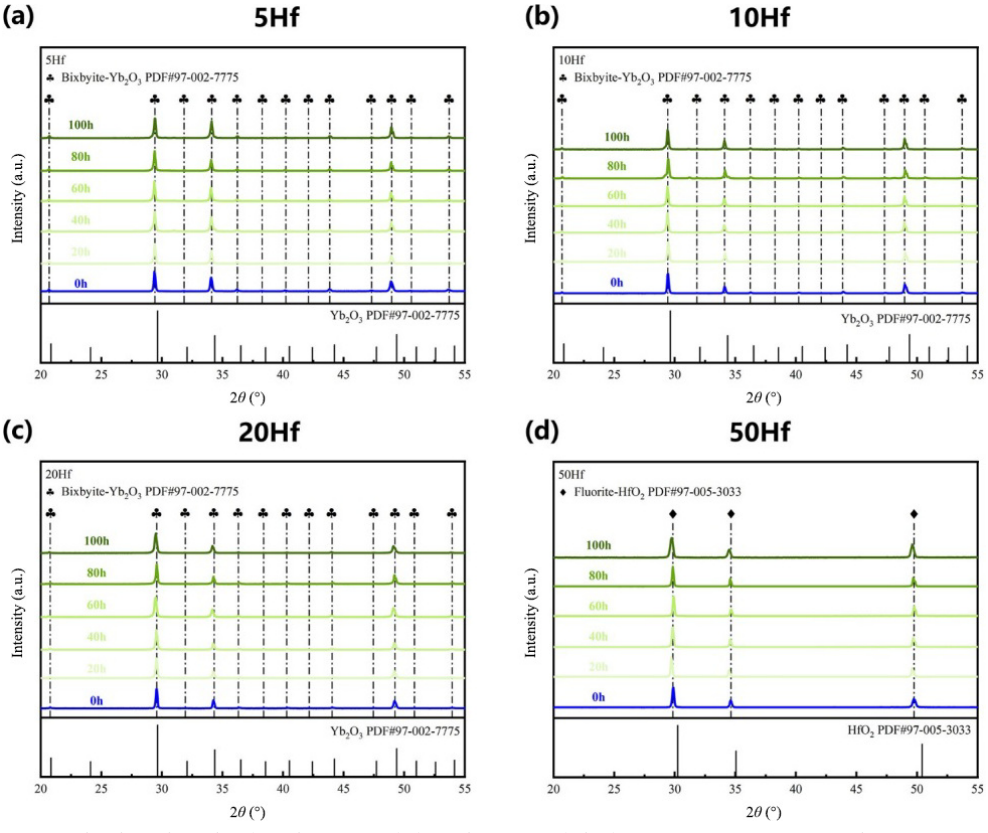

Fig. 9 XRD patterns of 5Hf, 10Hf, 20Hf, and 50Hf coatings with the surface removed after heat treatment at 1600 °C in air for 0, 20, 40, 60, 80, and 100 h.

configurational entropy on the phase stability of high-entropy oxides [14,36–38]. The configurational entropy (S_{config}) can be calculated using the Boltzmann formula (Eq. (4)):

$$S_{config} = k_B \ln \Omega \tag{4}$$

where k_B is the Boltzmann constant, and Ω represents the number of microscopic states accessible to the system.

$$\Omega = \Omega_1\Omega_2 \ldots \Omega_i = \frac{N_1!}{N_{11}! \ldots N_{1j}!} \cdots \frac{N_i!}{N_{i1}! \ldots N_{ij}!}$$
$$\approx \sum_i N_i \ln N_i - \sum_{ij} N_{ij} \ln N_{ij} \tag{5}$$

$$N_{ij} = x_{ij} N_i \tag{6}$$

where Ω_i denotes the number of available states for particle i, N_i represents the total quantity of particle i, N_{ij} corresponds to the number of particle i occupying lattice site j, and x_{ij} describes the occupation probability of particle i residing in type lattice site j. The corresponding configurational entropy is given by (Eq. (7)):

$$S_{config} = -k_B \sum_i \left(N_i \sum_j x_{ij} \ln x_{ij} \right) \tag{7}$$

In $(RE_{1-x}Hf_x)_2O_{3+x}X_{1-x}$ solid solutions, the configurational entropy can be analyzed by considering two distinct contributions: cationic (Y, Ho, Er, Yb, and Hf) and anionic (O and vacancies) arrangements. Figure 10 illustrates the evolution of configurational entropy in $(RE_{1-x}Hf_x)_2O_{3+x}X_{1-x}$ solid solutions as a function of HfO_2 doping content. The configurational entropies of both the bixbyite and fluorite structures are systematically calculated for all constituent components, although some scenarios are practically impossible. In the bixbyite structure, with increasing HfO_2 doping

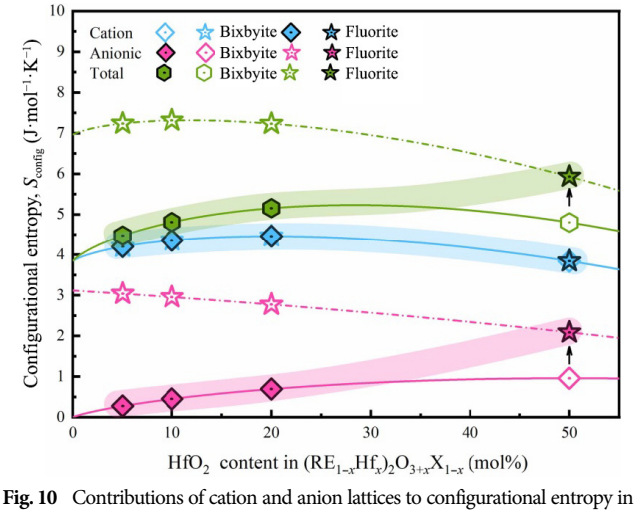

Fig. 10 Contributions of cation and anion lattices to configurational entropy in $(RE_{1-x}Hf_x)_2O_{3+x}X_{1-x}$ with various HfO_2 doping contents.

content, the cationic configurational entropy initially rises, reaching a maximum at 20 mol% HfO_2, where the atomic ratios of Y, Ho, Er, Yb, and Hf are equimolar, thereby maximizing entropy. In contrast, the anionic configurational entropy increases monotonically with HfO_2 doping. However, due to the substantially smaller magnitude of the anionic contribution compared to its cationic counterpart, the total configurational entropy is overwhelmingly dominated by the cationic arrangement, closely following its trend. Notably, the 50Hf coating exhibits a fluorite structure rather than bixbyite. Although the cationic configurational entropy is identical in these two phases (owing to complete cationic disorder in each), the bixbyite-to-fluorite transition introduces significant anionic disorder. This disordered anion sublattice substantially enhances the total

configurational entropy, resulting in a pronounced increase. In summary, the configurational entropy increases progressively with HfO_2 doping, thereby enhancing the high-temperature phase stability of the material. In particular, the random distribution of anions in the fluorite phase plays a particularly crucial role.

3.6 Thermal conductivity

The thermal resistance of a coating, governed by its low thermal conductivity, is crucial for sustaining performance in high-temperature environments. Figures 11(a) and 11(b) depict the temperature-dependent variations in the calculated heat capacity and measured thermal diffusivity, respectively. The thermal conductivity, derived from Eq. (1), is presented in Fig. 11(c). Theoretically, the thermal conductivity of dielectric solids should follow a $1/T$ trend owing to anharmonic Umklapp phonon scattering [39]. However, the experimental data deviate from this behavior at elevated temperatures. This discrepancy arises from increased laser transmittance in the dense oxide coatings at higher temperatures, enhancing radiative transport and consequently affecting the thermal diffusivity measurement [40]. For the 5Hf sample, the thermal conductivity is approximately 1.90 $W{\cdot}m^{-1}{\cdot}K^{-1}$ at room temperature. As the temperature increases to 1200 °C, it decreases to 1.17 $W{\cdot}m^{-1}{\cdot}K^{-1}$, but upon further heating to 1600 °C, a slight recovery to 1.22 $W{\cdot}m^{-1}{\cdot}K^{-1}$ is observed. In contrast, the 10Hf, 20Hf, and 50Hf samples demonstrate lower room-temperature thermal conductivities of 1.48, 1.03, and 0.60 $W{\cdot}m^{-1}{\cdot}K^{-1}$, respectively. The thermal conductivity reached its lowest values (1.06, 0.77, and 0.52 $W{\cdot}m^{-1}{\cdot}K^{-1}$) at 800 °C. Subsequent heating to 1600 °C resulted in a moderate increase, with thermal conductivity values recovering to 1.07, 0.97, and 0.76 $W{\cdot}m^{-1}{\cdot}K^{-1}$, respectively. In comparison to $Yb_2Si_2O_7$ and Yb_2SiO_5, with room-temperature thermal conductivities of 3.50 and 2.63 $W{\cdot}m^{-1}{\cdot}K^{-1}$, which are commonly used as intermediate layers in T/EBC systems, $(RE_{1-x}Hf_x)_2O_{3+x}X_{1-x}$ solid solutions exhibit significantly improved thermal insulation properties.

Overall, the thermal conductivity of $(RE_{1-x}Hf_x)_2O_{3+x}X_{1-x}$ solid solutions exhibits a gradual decrease with increasing HfO_2 doping content. This behavior primarily originates from enhanced phonon scattering with the lattice. According to the phonon gas model [41], the thermal conductivity (κ) can be expressed as (Eqs. (8) and (9)):

$$\kappa = \frac{1}{3} C_V v_g l \tag{8}$$

$$l = \frac{v_g}{\tau^{-1}} \tag{9}$$

where C_V, v_g, l, and τ^{-1} denote the volumetric heat capacity, group velocity, phonon mean free path, and phonon scattering rate, respectively. The enhanced scattering rate substantially suppresses the lattice thermal conductivity by reducing the phonon mean free path. τ^{-1} can be further described using the Matthiessen rule (Eq. (10)) [21]:

$$\tau^{-1} = \tau_U^{-1} + \tau_D^{-1} + \tau_B^{-1} + \tau_{ph\text{-}e}^{-1} \tag{10}$$

where τ_U^{-1}, τ_D^{-1}, τ_B^{-1}, and $\tau_{ph\text{-}e}^{-1}$ denote the Umklapp scattering rate, point defect scattering rate, grain boundary scattering rate, and phonon-electron scattering rate, respectively. Given that $(RE_{1-x}Hf_x)_2O_{3+x}X_{1-x}$ maintains analogous crystal structures, exhibits insulating electronic properties, and has grain sizes substantially larger than the phonon mean free path, the τ_U^{-1}, τ_B^{-1}, and $\tau_{ph\text{-}e}^{-1}$ terms can be excluded from the discussion. The point-defect scattering rate can be determined as (Eq. (11)) [42]:

$$\tau_D^{-1} = \frac{V\omega^4}{4\pi v_g^3} \Gamma \tag{11}$$

where V, ω, and Γ denote the volume per atom, frequency of the phonon mode, and disorder parameter, respectively. The disorder induced by point defects primarily stems from two contributions: mass fluctuations and size fluctuation, which are given by (Eqs. (12)–(15)) [43,44]:

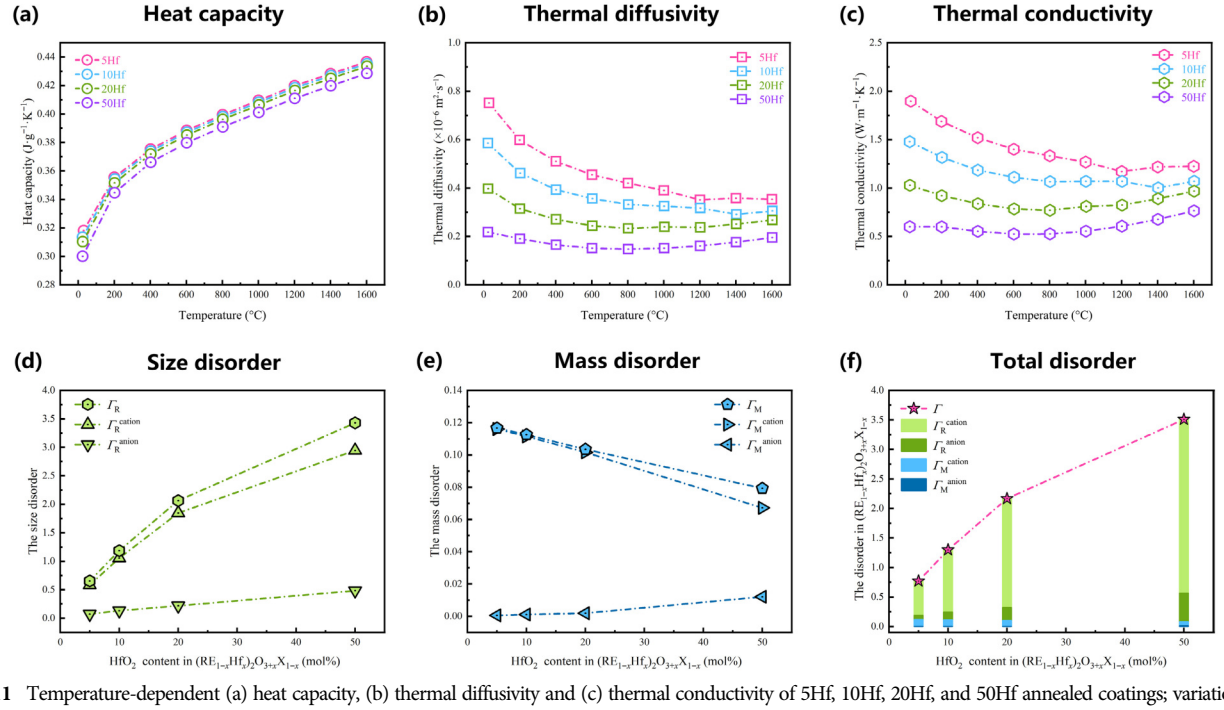

Fig. 11 Temperature-dependent (a) heat capacity, (b) thermal diffusivity and (c) thermal conductivity of 5Hf, 10Hf, 20Hf, and 50Hf annealed coatings; variations in (d) size, (e) mass and (f) total disorder in $(RE_{1-x}Hf_x)_2O_{3+x}X_{1-x}$ with HfO_2 doping content.

$$\Gamma_M = \sum_i \frac{g^i}{g}\left(\frac{\overline{M}^i}{\overline{M}}\right)^2 \Gamma_M^i \quad (12)$$

$$\Gamma_M^i = \sum_k c_k\left(1-\frac{M_k^i}{\overline{M}^i}\right)^2 \quad (13)$$

$$\Gamma_R = \varepsilon\sum_i \frac{g^i}{g}\left(\frac{\overline{R}^i}{\overline{R}}\right)^2 \Gamma_R^i \quad (14)$$

$$\Gamma_R^i = \sum_k c_k\left(1-\frac{R_k^i}{\overline{R}^i}\right)^2 \quad (15)$$

where i represents the independent crystallographic site. g and g^i denote the i-site and total degeneracy, respectively. $\overline{M}^i$, $\overline{M}$, $\overline{R}^i$, and $\overline{R}$ represent the average mass and ion radius of the whole crystal and the selected crystallographic site, respectively. Γ_M^i and Γ_R^i denote the disorders induced by mass and size fluctuations. M_k^i and R_k^i represent the mass and radius of k atom in i crystallographic site. c_k is the fraction of k atoms occupying the i crystallographic site. The parameter ε represents a phenomenologically adjustable parameter that characterizes the lattice anharmonicity. Its value is determined by the Grüneisen constant (γ) and the Poisson's ratio (μ) [44].

$$\varepsilon = 2\left(\frac{2\gamma}{\sqrt{6}}+\frac{6.4}{3}\gamma\frac{1+\mu}{1-\mu}\right)^2 \quad (16)$$

The bixbyite-type solid solution $(RE_{1-x}Hf_x)_2O_{3+x}X_{1-x}$ possesses four independent crystallographic sites, RE/Hf_{24d}, RE/Hf_{8b}, O_{48e}, and O/X_{16c}, with respective degeneracies of 3, 1, 6, and 2. The disorder induced by mass fluctuations is given by (Eq. (17)):

$$\begin{aligned}\Gamma_M(\text{bixbyite}) = {} & \frac{3}{12}\left(\frac{\overline{M}^{RE/Hf_{24d}}}{\overline{M}}\right)^2 \Gamma_M^{RE/Hf_{24d}} \\ & + \frac{1}{12}\left(\frac{\overline{M}^{RE/Hf_{8b}}}{\overline{M}}\right)^2 \Gamma_M^{RE/Hf_{8b}} \\ & + \frac{6}{12}\left(\frac{\overline{M}^{O_{48e}}}{\overline{M}}\right)^2 \Gamma_M^{O_{48e}} + \frac{2}{12}\left(\frac{\overline{M}^{X_{16c}}}{\overline{M}}\right)^2 \Gamma_M^{O/X_{16c}}\end{aligned} \quad (17)$$

where Y, Ho, Er, Yb, and Hf cations are uniformly distributed over the RE/Hf_{24d} and RE/Hf_{8b} sites with equal occupancy; thus, $\Gamma_M^{RE/Hf_{24d}} = \Gamma_M^{RE/Hf_{8b}} = \Gamma_M^{RE/Hf}$, while the O_{48e} site is fully occupied by oxygen anions; thus, $\Gamma_M^{O_{48e}} = 0$. The mass fluctuation disorder in the bixbyite phase can be simplified as (Eq. (18)):

$$\Gamma_M(\text{bixbyite}) = \frac{1}{3}\left(\frac{\overline{M}^{RE/Hf}}{\overline{M}}\right)^2 \Gamma_M^{RE/Hf} + \frac{1}{6}\left(\frac{\overline{M}^{O/X_{16c}}}{\overline{M}}\right)^2 \Gamma_M^{O/X_{16c}} \quad (18)$$

Similarly, the expression for size fluctuation disorder in the bixbyite phase can be derived as Eq. (19):

$$\Gamma_R(\text{bixbyite}) = \frac{1}{3}\varepsilon\left(\frac{\overline{M}^{RE/Hf}}{\overline{M}}\right)^2 \Gamma_R^{RE/Hf} + \frac{1}{6}\varepsilon\left(\frac{\overline{M}^{O/X_{16c}}}{\overline{M}}\right)^2 \Gamma_R^{O/X_{16c}} \quad (19)$$

The fluorite-type solid solution merely contains two crystallographic sites: RE/Hf_{4a} and O/X_{8c}, with respective degeneracies of 1 and 2. The mass and size fluctuation disorders in the fluorite phase are expressed as (Eqs. (20) and (21)):

$$\Gamma_M(\text{fluorite}) = \frac{1}{3}\left(\frac{\overline{M}^{RE/Hf}}{\overline{M}}\right)^2 \Gamma_M^{RE/Hf} + \frac{2}{3}\left(\frac{\overline{M}^{O/X_{8c}}}{\overline{M}}\right)^2 \Gamma_M^{O/X_{8c}} \quad (20)$$

$$\Gamma_R(\text{fluorite}) = \frac{1}{3}\varepsilon\left(\frac{\overline{M}^{RE/Hf}}{\overline{M}}\right)^2 \Gamma_R^{RE/Hf} + \frac{2}{3}\varepsilon\left(\frac{\overline{M}^{O/X_{8c}}}{\overline{M}}\right)^2 \Gamma_R^{O/X_{8c}} \quad (21)$$

Equations (18)–(21) demonstrate that mass and size disorder in bixbyite- and fluorite-type solid solutions can be decoupled into two independent components: cation lattice and anion lattice contributions. Figures 11(d)and 11(e) illustrate the compositional dependence of these lattice disorders in $(RE_{1-x}Hf_x)_2O_{3+x}X_{1-x}$ solid solutions. For mass disorder, increasing the HfO_2 doping content results in a monotonic reduction in cation lattice disorder while simultaneously inducing an increase in anion lattice disorder, as evidenced in Fig. 11(d). Crucially, the total mass disorder is primarily dominated by cation doping, with the contribution from anion lattice disorder being negligible. For size disorder, both cation and anion lattice disorder intensify with higher HfO_2 doping content, as shown in Fig. 11(e). However, similar to the mass disorder case, the anion lattice contribution to the total size disorder remains marginal. Figure 11(f) further compares the total disorder in $(RE_{1-x}Hf_x)_2O_{3+x}X_{1-x}$ solid solutions along with the relative contributions from its size and mass components. This demonstrates that size disorder dominates the total disorder characteristics in the bixbyite and fluorite phases, accounting for > 85% of the total disorder across the composition range. The comprehensive analysis reveals that HfO_2 incorporation in $(RE_{1-x}Hf_x)_2O_{3+x}X_{1-x}$ solid solutions induces substantial cation size disorder, which strongly enhances phonon scattering through strain field effects, resulting in a dramatic reduction in thermal conductivity.

3.7 Thermal expansion

Thermal expansion compatibility in T/EBC systems plays a critical role in mitigating stress accumulation during thermal cycling, which is essential for ensuring long-term coating durability. A comprehensive understanding of the thermal expansion characteristics of these coatings is therefore imperative. Figure 12(a) presents the temperature-dependent line expansion rate in the 5Hf, 10Hf, 20Hf, and 50Hf coatings over an extensive temperature range (RT–1500 °C). The $\Delta L/L$ curves demonstrate quasilinear thermal expansion at low temperatures, evolving into a distinctly nonlinear response at elevated temperatures. The nonlinear behavior originates from the anharmonic characteristics of atomic vibrations [45]. In the low-temperature regime, where atomic vibrations approach harmonic behavior, the thermal expansion coefficient remains nearly constant. However, as the temperature rises, the growing influence of anharmonic interactions, which are driven by large-amplitude atomic vibrations, induces a slight increase in the thermal expansion coefficient. The mean linear coefficients of thermal expansion of the 5Hf, 10Hf, 20Hf and 50Hf coatings are determined to be 8.92×10^{-6}, 9.14×10^{-6}, 9.81×10^{-6}, and 10.60×10^{-6} K^{-1}, respectively, through linear fitting of their respective $\Delta L/L$ curves. Although $(RE_{1-x}Hf_x)_2O_{3+x}X_{1-x}$ exhibits a higher thermal expansion coefficient than SiC_f/SiC CMCs ($(4.5–5.5)\times10^{-6}$ K^{-1}) [46], Si ($(3.5–4.5)\times10^{-6}$ K^{-1}) [46] or Si–HfO_2 ($(4.0–6.0)\times10^{-6}$ K^{-1}) [47] bond coats and rare earth silicate ($(4.0–8.0)\times10^{-6}$ K^{-1}) [46,48] intermediate layers are typically

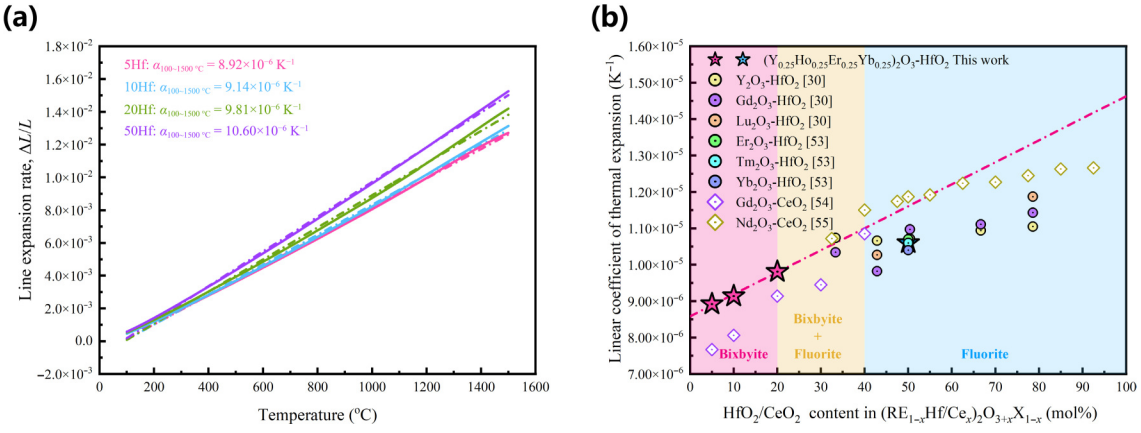

Fig. 12 (a) Temperature-dependent line expansion rate of 5Hf, 10Hf, 20Hf, and 50Hf annealed coatings. (b) Comparison of average linear thermal expansion coefficients in RE_2O_3–Hf/CeO_2 systems.

incorporated beneath the $(RE_{1-x}Hf_x)_2O_{3+x}X_{1-x}$ topcoats in practical applications. This gradient structural design serves to mitigate thermal stress accumulation during thermal cycling, thereby guaranteeing coating durability and service life.

The thermal expansion coefficient of $(RE_{1-x}Hf_x)_2O_{3+x}X_{1-x}$ solid solutions demonstrates a pronounced compositional dependence, increasing systematically with HfO_2 doping content, as evidenced in Fig. 12(b). For isotropic materials, the linear expansion coefficient can be approximately expressed as Eq. (22):

$$\alpha_L \approx \frac{1}{3}\alpha_V \tag{22}$$

where α_L and α_V are the linear and volume thermal expansion coefficient, respectively. As described by the Grüneisen law [49], α_V is given by (Eq. (23)):

$$\alpha_V = \frac{\gamma}{B}\frac{C_V}{V} \tag{23}$$

where γ, B, C_V, and V denote the Grüneisen constant, bulk modulus, heat capacity at constant volume, and lattice volume, respectively. As evidenced by Figs. 6(e) and 11(a), the variations in heat capacity and volume induced by HfO_2 doping remained below 5%. The enlargement of the thermal expansion coefficient is primarily attributed to the terms γ and B. These two parameters represent the respective contributions of lattice anharmonicity and bond strength. The incorporation of small and tetravalent Hf ions enhances anion–cation bonding in the $(RE_{1-x}Hf_x)_2O_{3+x}X_{1-x}$ structure, as corroborated by the previously measured hardness and Young's modulus. Theoretically, such bond strengthening should result in a reduction in the thermal expansion coefficient, but experimental observations reveal the opposite trend. First-principles calculations demonstrated that the Grüneisen parameters of cubic hafnium oxide were considerably higher than those of rare earth oxides [50,51], and experimental results also confirmed that hafnium oxide possessed a higher thermal expansion coefficient [15,20,52]. These findings indicate that the introduction of Hf–O bonds will enhance the lattice anharmonicity and improve the thermal expansion coefficient. In the bixbyite phase, the thermal expansion coefficient exhibits a near-linear relationship with the HfO_2 concentration. However, the linearity is disrupted once the structure transforms to the fluorite phase, where the measured value deviates approximately 10% below the linear extrapolation from the bixbyite regime. This phenomenon extends beyond the $(Y_{0.25}Ho_{0.25}Er_{0.25}Yb_{0.25})_2O_3$–$HfO_2$ system investigated in this work, which has been consistently observed in numerous systems, including Y_2O_3–HfO_2 [30], Gd_2O_3–HfO_2 [30], Er_2O_3–HfO_2 [53], Tm_2O_3–HfO_2 [53], Yb_2O_3–HfO_2 [53], and Lu_2O_3–HfO_2 [30], as well as in Gd_2O_3–CeO_2 [54] and Nd_2O_3–CeO_2 [55] systems. The lattice anharmonicity is also influenced by the crystal structure. As previously discussed, the bixbyite-to-fluorite phase transition induces a structural reorganization: RE/Hf cations and O anions migrate to higher-symmetry 4a and 8c sites, respectively. This transition enhances crystal symmetry and offsets partial lattice anharmonicity introduced by Hf–O bonds. Thus, it shows an observed deviation from the initial trend.

4 Conclusions

This study systematically investigated the structural characteristics and thermophysical properties of hafnium-doped high-entropy $(Y_{0.25}Ho_{0.25}Er_{0.25}Yb_{0.25})_2O_3$ coatings deposited by APS. The key findings are summarized as follows:

(1) The $(RE_{1-x}Hf_x)_2O_{3+x}X_{1-x}$ coatings with low HfO_2 doping contents (5Hf, 10Hf, and 20Hf) maintain a cubic bixbyite structure, while the high HfO_2 doping content (50Hf) triggers a transition to a fluorite structure.

(2) The increase in HfO_2 doping content from 5 to 50 mol% resulted in a more than twofold improvement in material hardness (from 6.7±0.2 to 18.0±1.6 GPa) and Young's modulus (from 118.4±7.6 to 229±10.0 GPa). The introduction of Hf–O bonds strengthens the lattice resistance to elastic and plastic deformation.

(3) At 1600 °C, the 5Hf, 10Hf, and 20Hf coatings with bixbyite structures partially transform into a hexagonal RE_6HfO_{11} phase, whereas the fluorite-structure 50Hf coating demonstrates superior phase stability. The enhanced phase stability is attributed to the increased configurational entropy resulting from the ordered arrangement of oxygen anions and vacancies in the fluorite structure.

(4) The thermal conductivity of the $(RE_{1-x}Hf_x)_2O_{3+x}X_{1-x}$ coatings decreases significantly with HfO_2 doping content, and the 50Hf coating exhibits the lowest values (0.60 $W{\cdot}m^{-1}{\cdot}K^{-1}$ at room temperature and 0.76 $W{\cdot}m^{-1}{\cdot}K^{-1}$ at 1600 °C). The reduction of thermal conductivity is attributed to the enhanced phonon scattering from lattice distortions and point defects, with size disorder playing the dominant role.

(5) The thermal expansion coefficients of the bixbyite-structure 5Hf, 10Hf, and 20Hf coatings are 8.92×10^{-6}, 9.14×10^{-6}, and 9.81×10^{-6} K^{-1}, respectively, which increase linearly with HfO_2 doping content. However, the thermal expansion coefficient of the fluorite-structured 50Hf coating (10.60×10^{-6} K^{-1}) exhibits a deviation from this linear trend, which is related to the reduction

in lattice anharmonicity following the bixbyite-to-fluorite phase transition.

The demonstrated combination of progressively improved hardness and Young's modulus, enhanced phase stability, low thermal conductivity and tailored thermal expansion coefficient positions hafnium-doped high-entropy oxides $(Y_{0.25}Ho_{0.25}Er_{0.25}Yb_{0.25})_2O_3$ as potential candidates for advanced T/EBCs.

Acknowledgements

This work was financially supported by the National Key R&D Program of China (No. 2021YFB3702303) and the Industry-University-Research Cooperation Project of AECC (No. HFZL2023CXY022).

Availability of data and materials

The data that support the findings of this study are available from the corresponding author upon reasonable request.

Competing interests

The authors have no competing interests to declare that are relevant to the content of this article. The author Jingyang Wang is the Editorial Committee member of this journal.

Electronic Supplementary Material

Supplementary material is available in the online version of this article at https://doi.org/10.26599/JAC.2026.9221250.

References

[1] Song CK, Ye F, Cheng LF, *et al.* Long-term ceramic matrix composite for aeroengine. *J Adv Ceram* 2022, **11**: 1343–1374.

[2] Tejero-Martin D, Bennett C, Hussain T. A review on environmental barrier coatings: History, current state of the art and future developments. *J Eur Ceram Soc* 2021, **41**: 1747–1768.

[3] Fang GW, Gao XG, Song YD. A review on ceramic matrix composites and environmental barrier coatings for aero-engine: Material development and failure analysis. *Coatings* 2023, **13**: 357.

[4] Zhu DM, Advanced environmental barrier coatings for SiC–SiC ceramic matrix composite turbine components. In: *Engineered Ceramics: Current Status and Future Prospects*. Ohji T, Singh M, Eds. Hoboken: John Wiley & Sons, Inc., 2015: 187–202.

[5] Poerschke DL, Van Sluytman JS, Wong KB, *et al.* Thermochemical compatibility of ytterbia–(hafnia/silica) multilayers for environmental barrier coatings. *Acta Mater* 2013, **61**: 6743–6755.

[6] Spitsberg I, Steibel J. Thermal and environmental barrier coatings for SiC/SiC CMCs in aircraft engine applications. *Int J Appl Ceram Tec* 2004, **1**: 291–301.

[7] Lashmi PG, Ananthapadmanabhan PV, Unnikrishnan G, *et al.* Present status and future prospects of plasma sprayed multilayered thermal barrier coating systems. *J Eur Ceram Soc* 2020, **40**: 2731–2745.

[8] Poerschke DL, Hass DD, Eustis S, *et al.* Stability and CMAS resistance of ytterbium–silicate/hafnate EBCs/TBC for SiC composites. *J Am Ceram Soc* 2015, **98**: 278–286.

[9] Yin Q, Shen KH, Wang Y, *et al.* Research progress of rare earth zirconate thermal barrier coating ceramic materials. *Mater Today Commun* 2025, **42**: 111579.

[10] Iqbal A, Moskal G, Cavaleiro A, *et al.* The current advancement of zirconate based dual phase system in thermal barrier coatings (TBCs): New modes of the failures: Understanding and investigations. *Alex Eng J* 2024, **91**: 161–196.

[11] Zhao ZF, Chen H, Xiang HM, *et al.* High-entropy $(Y_{0.2}Nd_{0.2}Sm_{0.2}Eu_{0.2}Er_{0.2})AlO_3$: A promising thermal/environmental barrier material for oxide/oxide composites. *J Mater Sci Technol* 2020, **47**: 45–51.

[12] Liao W, Tan YQ, Teng Z, *et al.* High entropy $(Y_{1/5}Ho_{1/5}Er_{1/5}Yb_{1/5}Lu_{1/5})_3Al_5O_{12}$ with low thermal conductivity and high thermal stability. *J Alloys Compd* 2023, **949**: 169736.

[13] Chen L, Li BH, Feng J. Rare-earth tantalates for next-generation thermal barrier coatings. *Prog Mater Sci* 2024, **144**: 101265.

[14] Sarkar A, Breitung B, Hahn H. High entropy oxides: The role of entropy, enthalpy and synergy. *Scripta Mater* 2020, **187**: 43–48.

[15] Sun YN, Xiang HM, Dai FZ, *et al.* Preparation and properties of CMAS resistant bixbyite structured high-entropy oxides RE_2O_3 (RE = Sm, Eu, Er, Lu, Y, and Yb): Promising environmental barrier coating materials for Al_2O_{3f}/Al_2O_3 composites. *J Adv Ceram* 2021, **10**: 596–613.

[16] Ping XY, Meng B, Yu XH, *et al.* Structural, mechanical and thermal properties of cubic bixbyite-structured high-entropy oxides. *Chem Eng J* 2023, **464**: 142649.

[17] Ping XY, Meng B, Zeng WX, *et al.* Effects of element addition on the microstructure and thermophysical properties of seven-principal cations rare-earth high-entropy oxide. *J Mater Res Technol* 2024, **31**: 2217–2225.

[18] Shannon RD. Revised effective ionic radii and systematic studies of interatomic distances in halides and chalcogenides. *Acta Crystallogr A* 1976, **32**: 751–767.

[19] Duran P, Pascual C. Phase equilibria and ordering in the system HfO_2–Yb_2O_3. *J Mater Sci* 1984, **19**: 1178–1184.

[20] Haggerty RP, Sarin P, Apostolov ZD, *et al.* Thermal expansion of HfO_2 and ZrO_2. *J Am Ceram Soc* 2014, **97**: 2213–2222.

[21] Dugdale JS, Basinski ZS. Mathiessen's rule and anisotropic relaxation times. *Phys Rev* 1967, **157**: 552–560.

[22] Yin QH, Sun ZP, Wang JJ, *et al.* Research status of RE hafnates for thermal/environmental barrier coatings. *Ceram Int* 2025, **51**: 22987–23002.

[23] Information on https://ntrs.nasa.gov/api/citations/20050192261/downloads/20050192261.pdf.

[24] Barin I, Knacke O, Kubaschewski O. *Thermochemical Properties of Inorganic Substances*. Berlin, Heidelberg: Springer, 1977.

[25] Eslamian M, Ashgriz N. Spray drying, spray pyrolysis and spray freeze drying. In: *Handbook of Atomization and Sprays*. Boston, Springer USA, 2010: 849–860.

[26] Sharma A, Witz G, Howell PC, *et al.* Interplay of the phase and the chemical composition of the powder feedstock on the properties of porous 8YSZ thermal barrier coatings. *J Eur Ceram Soc* 2021, **41**: 3706–3716.

[27] Vehring R. Pharmaceutical particle engineering via spray drying. *Pharm Res* 2008, **25**: 999–1022.

[28] Andrievskaya ER, Lopato LM, Smirnov VP. The system HfO_2–Y_2O_3–Er_2O_3. *J Am Ceram Soc* 1996, **79**: 714–720.

[29] Shevchenko AV, Lopato LM, Kir'yakova IE. Interaction of HfO_2 with Y_2O_3, Ho_2O_3, Er_2O_3, Tm_2O_3, Yb_2O_3 and Lu_2O_3 at high temperatures. *Izv An SSSR* 1984, **20**: 1991–1996.

[30] Sévin L, Audouard L, Razafindramanana V, *et al.* Phase stabilisation, thermal expansion and ionic conductivity of high content rare earth oxide (Lu_2O_3, Y_2O_3 and Gd_2O_3) stabilised cubic hafnia. *J Eur Ceram Soc* 2023, **43**: 4153–4166.

[31] Spiridigliozzi L, Monfreda V, Marocco A, *et al.* On the effect of kinetics on the formation of fluorite/bixbyite-structured entropy-stabilized oxides. *Ceram Int* 2025, **51**: 30684–30692.

[32] Yashima M, Ishizawa N, Yoshimura M. Application of an ion-packing model based on defect clusters to zirconia solid solutions: II, applicability of vegard's law. *J Am Ceram Soc* 1992, **75**: 1550–1557.

[33] Pascual C, Durán P. Subsolidus phase equilibria and ordering in the system ZrO_2–Y_2O_3. *J Am Ceram Soc* 1983, **66**: 23–27.

[34] Liu XQ, Mi JX, Shi L, *et al. In situ* modulation of A-site vacancies in $LaMnO_{3.15}$ perovskite for surface lattice oxygen activation and boosted redox reactions. *Angew Chem-Ger Edit* 2021, **60**: 26747–26754.

[35] He Y, Zhang L, Xiong HW, *et al.* Evolution of lattice defects in nickel ferrite spinel: Oxygen vacancy and cation substitution. *J Alloys Compd* 2022, **917**: 165494.

[36] Miracle DB, Senkov ON. A critical review of high entropy alloys and related concepts. *Acta Mater* 2017, **122**: 448–511.
[37] Dippo OF, Vecchio KS. A universal configurational entropy metric for high-entropy materials. *Scripta Mater* 2021, **201**: 113974.
[38] Fracchia M, Coduri M, Ghigna P, *et al.* Phase stability of high entropy oxides: A critical review. *J Eur Ceram Soc* 2024, **44**: 585–594.
[39] Berman R. The thermal conductivity of dielectric solids at low temperatures. *Adv Phys* 1953, **2**: 103–140.
[40] Winter MR, Clarke DR. Oxide materials with low thermal conductivity. *J Am Ceram Soc* 2007, **90**: 533–540.
[41] Lv W, Henry A. Examining the validity of the phonon gas model in amorphous materials. *Sci Rep-UK* 2016, **6**: 37675.
[42] Klemens PG. The scattering of low-frequency lattice waves by static imperfections. *P Phys Soc Lond A* 1955, **68**: 1113–1128.
[43] Slack GA. Thermal conductivity of MgO, Al_2O_3, $MgAl_2O_4$, and Fe_3O_4 Crystals from 3° to 300° K. *Phys Rev* 1962, **126**: 427–441.
[44] Abeles B. Lattice thermal conductivity of disordered semiconductor alloys at high temperatures. *Phys Rev* 1963, **131**: 1906–1911.
[45] Jasrasaria D, Berkelbach TC. Nonperturbative simulation of anharmonic rattler dynamics in type-I clathrates with vibrational dynamical mean-field theory. *Phys Rev B* 2024, **110**: 064312.
[46] Lee KN, Fox DS, Bansal NP. Rare earth silicate environmental barrier coatings for SiC/SiC composites and Si_3N_4 ceramics. *J Eur Ceram Soc* 2005, **25**: 1705–1715.
[47] Harder BJ. Oxidation performance of Si–HfO_2 environmental barrier coating bond coats deposited via plasma spray-physical vapor deposition. *Surf Coat Tech* 2020, **384**: 125311.
[48] Tian ZL, Zheng LY, Wang JM, *et al.* Theoretical and experimental determination of the major thermo-mechanical properties of RE_2SiO_5 (RE=Tb, Dy, Ho, Er, Tm, Yb, Lu, and Y) for environmental and thermal barrier coating applications. *J Eur Ceram Soc* 2016, **36**: 189–202.
[49] Liu ZJ, Song T, Sun XW, *et al.* Thermal expansion, heat capacity and Grüneisen parameter of iridium phosphide Ir_2P from quasi-harmonic Debye model. *Solid State Commun* 2017, **253**: 19–23.
[50] Hoat DM, Rivas Silva JF, Blas AM. First principles study of structural, electronic, elastic and thermodynamic properties of cubic HfO_2 under pressure. *Physica B* 2018, **545**: 55–61.
[51] Chu KL, Zhang YN, Liu BS, *et al.* Structural basis and bonding mechanisms for mechanical and thermal properties of rare earth oxides. *J Am Ceram Soc* 2025, **108**: 20305.
[52] Zhang GH, Zhang J, Wang JY. Synthesis and characterization of ytterbium oxide: A novel CMAS-resistant environmental barrier coating material. *J Am Ceram Soc* 2023, **106**: 621–631.
[53] Guskov AV, Gagarin PG, Guskov VN, *et al.* Thermal properties of solid solutions $Ln_2O_3{\cdot}2HfO_2$ (Ln = Dy, Ho, Er, Tm, Yb, Lu) at 300–1300 K. *Ceram Int* 2021, **47**: 28004–28007.
[54] Grover V, Tyagi AK. Phase relations, lattice thermal expansion in CeO_2–Gd_2O_3 system, and stabilization of cubic gadolinia. *Mater Res Bull* 2004, **39**: 859–866.
[55] Chavan SV, Mathews MD, Tyagi AK. Phase relations and thermal expansion studies in the CeO_2–$NdO_{1.5}$ system. *Mater Res Bull* 2005, **40**: 1558–1568.